HHS Public Access

Author manuscript

ACS Sens. Author manuscript; available in PMC 2019 November 05.

Published in final edited form as:

ACS Sens. 2018 August 24; 3(8): 1510–1521. doi:10.1021/acssensors.8b00301.

Kernel-Based Microfluidic Constriction Assay for Tumor Sample Identification

Xiang Ren[†], **Parham Ghassemi**[†], **Yasmine M. Kanaan**[‡], **Tammey Naab**[§], **Robert L. Copeland**[‖], **Robert L. Dewitty**[⊥], **Inyoung Kim**[▽], **Jeannine S. Strobl**[†], **Masoud Agah**[*,†]

[†]The Bradley Department of Electrical and Computer Engineering, Virginia Tech, Blacksburg, Virginia 24061, United States

[‡]Microbiology Department, Howard University, College of Medicine, Cancer Center, Washington, DC 20059, United States

[§]Pathology Department, Howard University, College of Medicine, Cancer Center, Washington, DC 20059, United States

[‖]Pharmacology Department, Howard University, College of Medicine, Cancer Center, Washington, DC 20059, United States

[⊥]Howard University Hospital, Providence Hospital, Washington, DC 20017, United States

[▽]Department of Statistics, Virginia Tech, Blacksburg, Virginia 24061, United States

Abstract

A high-throughput multiconstriction microfluidic channels device can distinguish human breast cancer cell lines (MDA-MB-231, HCC-1806, MCF-7) from immortalized breast cells (MCF-10A) with a confidence level of ~81–85% at a rate of 50–70 cells/min based on velocity increment differences through multiconstriction channels aligned in series. The results are likely related to the deformability differences between nonmalignant and malignant breast cells. The data were analyzed by the methods/algorithms of Ridge, nonnegative garrote on kernel machine (NGK), and Lasso using high-dimensional variables, including the cell sizes, velocities, and velocity increments. In kernel learning based methods, the prediction values of 10-fold cross-validations are used to represent the difference between two groups of data, where a value of 100% indicates the two groups are completely distinct and identifiable. The prediction value is used to represent the difference between two groups using the established algorithm classifier from high-dimensional variables. These methods were applied to heterogeneous cell populations prepared using primary tumor and adjacent normal tissue obtained from two patients. Primary breast cancer cells were distinguished from patient-matched adjacent normal cells with a prediction ratio of

[*]**Corresponding Author:** agah@vt.edu.

Author Contributions

The manuscript was written through contributions of all authors. All authors have given approval to the final version of the manuscript.

Supporting Information

The Supporting Information is available free of charge on the ACS Publications website at DOI:10.1021/acssensors.8b00301.

Human subjects and clinical data and patient sample preparation and postexperiment collection; fabrication processes; breast Cell lines video/image; verification of the identity of cells as cancer versus nontumorigenic (MCF-10A) at the single cell level; full table of prediction values (PDF) example of the cells passing through the channels (AVI)

The authors declare no competing financial interest.

70.07%–75.96% by the NGK method. Thus, this high-throughput multiconstriction microfluidic device together with the kernel learning method can be used to perturb and analyze the biomechanical status of cells obtained from small primary tumor biopsy samples. The resultant biomechanical velocity signatures identify malignancy and provide a new marker for evaluation in risk assessment.

Graphical Abstract

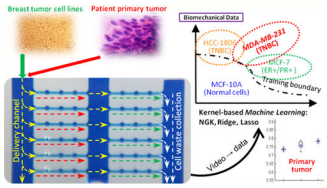

Keywords

breast cancer cells; kernel learning; multiconstriction microfluidic channels; machine learning; variable selection; patient primary tumor cells

The determination of risk for a patient with a primary tumor of the breast is of utmost interest to patients and clinicians alike. Clinical, pathological, biochemical, and most recently genetic tests have been developed in an attempt to inform treatment decisions based upon the risk for tumor metastasis and postsurgical recurrence rates. Tumors with aggressive markers will require adjuvant therapies, but in other primary tumors and conditions such as ductal carcinoma in situ (DCIS) more indolent markers are present. In such patients, there is still uncertainty what additional therapy beyond surgical resection is warranted or if no further therapy would be more appropriate in which case, physicians risk overtreatment of a nonaggressive condition.

Biomechanical properties of metastatic cancer cells provide a clue that the study of biomechanics of primary tumor cells might be of use as a marker of risk in primary breast cancer. Studies of cell lines derived from metastatic breast cancer show such cells have softer biomechanical strength, based on their cytoskeleton, microtubules and actin filaments, which result in a higher deformability in microfluidic constriction channels.[1–3] Microfluidic devices utilizing constriction channels have been broadly applied to metastatic studies on different cell lines.[4–8] Many studies have demonstrated the utility of circulating tumor cells as a minimally invasive cancer screening method for both the initial diagnosis of cancer and in monitoring patients for recurrent or metastatic cancer.[9,10] An essential step in escape from the primary tumor is the epithelial-mesenchymal transition (EMT) that allows cancer cells to become more motile and more likely to survive in the patient circulation. Most of the studies on the mechanical properties of cell lines at single-cell level have been carried out in a single constriction microfluidic channel.[4,5,11,12] Here, we show using an array of multiconstriction microfluidic channels a higher throughput is achieved. The multiple constriction channels can generate multiple deformations to cell structure, which increases the velocity-related variables for mechanical behavior analysis that can be correlated to metastatic characteristics.[2,13]

Multiple technologies have confirmed the biomechanical softness is most pronounced in the more metastatic prone cell lines. Such technologies include atomic force microscopy (AFM),[14–17] micropipet aspiration,[18–20] optical deformability,[21,22] and magnetic beads with selective antibodies assays.[23] For clinical applications, the high-throughput of microfluidic approaches and lab-on-chip technologies are more attractive. What is unknown is how the biomechanical properties of breast cells derived from primary tumors in patients and breast cells grown in long-term culture compare. Here, we show in a multiconstriction microfluidic device that patient-derived primary human breast tumor cells and breast cell lines show similar incremental velocity profiles, providing proof-of-concept that biomechanical properties of primary tumors can be assessed. Furthermore, the primary tumor tissue is biomechanically distinguishable from the patient's own adjacent normal breast tissue. This work represents an important development in microfluidic analysis of breast biopsies and how cell biomechanical properties might contribute to the assessment of patient risk.

EXPERIMENTAL SECTION

Materials and Methods.

Cell Culture and Sample Preparation.—MDA-MB-231 cells (passage #6, American Type Culture Collection (ATCC), Manassas, VA) were grown in F12:DMEM (Lonza, Basel, Switzerland) with 10% fetal bovine serum (FBS), 4 mM glutamine, and penicillin-streptomycin (100 units per mL). HCC-1806 cells (passage #5, ATCC) were grown in ATCC-formulated RPMI-1640 medium with 10% FBS. MCF-7 cells (passage #5, ATCC) were grown in EMEM with 10% FBS, and 2× L-glutamine. MCF-10A cells (passage #19, Lombardi Comprehensive Cancer Center, Georgetown University in Washington, DC were grown in F12:DMEM with penicillin-streptomycin (100 units per mL), 2.5 mM L-glutamine, 20 ng/mL epidermal growth factor (EGF), 0.1 μg/mL cholera toxin, 10 μg/mL insulin, 0.5 μg/mL hydrocortisone, and 5% horse serum. All of the cells were grown in T-25 cm^2 culture flasks at 37 °C in a 5% CO_2 in air atmosphere until cells were ready for subculture. The morphology of the cells was observed before trypsinization. The cells were then detached from the flask with trypsin-EDTA solution (SigmaAldrich). The MDA-MB-231, HCC-1806, MCF-7, and MCF-10A cells were trypsinized at 37 °C for 2, 8, 7, and 15 min, respectively. All of the cells were diluted to a final count of ~4×10^4cells/mL.

Human Subjects and Clinical Data.—For this study, two fresh breast tissue samples were collected along with clinical/pathological information with Institutional Review Board approval (IRB#2016–0601) from the Pathology Department at Providence Hospital and samples were coded to preserve patient confidentiality. Tumor diagnoses were confirmed by routine histopathological examination. (Detailed information available in the Supporting Information.)

Patient Sample Preparation and Postexperiment Collection.—The patient samples were frozen and transported from Howard Cancer Center to Virginia Tech. The thawing procedure for patient samples was different from the thawing of cell lines. Unlike the quick thawing procedure for cell lines, the patient samples in vials needed to be thawed slowly. The frozen samples were transferred to an ice pack for 10–15 min, followed by 4 °C fridge

for 10 min, and to room temperature until the samples melted. Then the vials were moved to a 37 °C water bath. The cancer samples were diluted with culture medium to reach the required cell concentration for microfluidic experiments.

After experiments, the patients' samples were collected from the sample collection outlet of the microfluidic device and stained for the epithelial markers (e.g., Pancytokeratin, CD45, CD68). (Detailed information available in the Supporting Information.)

Device Fabrication.—The microfluidic channels were fabricated by polydimethylsiloxane (PDMS) soft-lithography, followed by PDMS-glass bonding after plasma treatment. The molds for microfluidic channels were fabricated on a silicon wafer with two layers of SU-8 (SU-8 3005 and SU-8 3025, MicroChem, Newton, MA) photolithography. The detailed fabrication procedures are presented in the Supporting Information.

Experimental Setup.

The multiconstriction microfluidic channel array was treated with EDTA before experiment for 30 min to reduce the chance of cells attaching to the microchannel surfaces. Then, the device was washed with cell culturing medium to remove the residuals. The microfluidic device was mounted on an inverted microscope (Zeiss Axio Observer LSM-510, Thornwood, NY) with a 20X lens. The cell sample was connected to the inlet of the delivery channel. A constant pressure on the sample reservoir of 100 mbar was applied by a pressure pump. A negative pressure of 150 mbar was applied at the cell outlet collection channel. The pressure on the cell sample was kept constant during all the experiments on both cell lines and patient samples. Instead of using a high speed camera, a smartphone with slow motion function was used to record videos of the cell movement at a frame rate of 240 frames per second (fps). The overall magnification is 200X in smartphone video with a 1920 X 1080 resolution. The velocity information on the cells was extracted from the video using tracking software named "Tracker" (developed by "Open Source Physics", supported by the National Science Foundation). An example of a cell passing through the device is demonstrated in Supporting Information Figure S1. After the experiment on patients' cancer and adjacent normal samples, the used cells were collected at the outlet for secondary hematoxylin and eosin (H&E) staining studies. The cells were collected into vials, and 5% (v/v) DMSO was added into the vial for freezing purpose. The vials were frozen at −18 °C for 1 h before transferred into −80 °C freezer. The following H&E staining was performed at Howard Cancer Center.

Statistical Analysis.

We conduct variable selections and then obtain the prediction accuracy using 10-fold cross-validations. Three methods based on Ridge,[24] Lasso,[25] and NGK[26] methods are compared. Ridge and Lasso methods are popular variable selections methods based on multivariate linear and additive model, while NGK is a variable selection based on a nonlinear and nonparametric multivariate model. Ridge regression has been used the most popular when the data is not sparse, while Lasso has been used when the data is sparse. However, both methods are developed using multivariate linear and additive model. Hence, these two

methods are not appropriate when variables are interacted and highly correlated. Since NGK is developed under the nonlinear and nonadditive model, it automatically built the complex interaction among variables using kernel function. The main advantage of this kernel-based approach is very flexible: (1) it can automatically identify what variables are most significant; (2) it can automatically model unknown and complicated interactions; (3) it provides flexibility for both additive and nonadditive nonparametric models; (4) it also provides flexibility for both parametric and nonparametric model. That is, if there are no complicated interactions or nonparametric model, it automatically becomes additive model or parametric model.

RESULTS

Cell Lines.

The morphologies of two human triple-negative breast cancer (TNBC) cell lines, MDA-MB-231 and HCC-1806, the endocrine-responsive (ER+/PR+/Her2−) MCF-7 cell line, and the immortalized breast epithelial cell line MCF-10A used in these studies are shown in Figure 1. Their cell sizes measured as the longest axial dimension were determined from video recorded images of the cells entering the microfluidic channel using a smartphone with slow-motion setting on an inverted microscope. The difference between the smartphone and a high-speed camera, such as IDT Redlake NX-3 (IDT vision, Pasadena, CA)[1,2,27,28] that we have in the lab, is the available memory and the subsequent time we can record the videos without interrupting the experiment. A smartphone used in this work has an internal memory of 64GB while the high-speed camera provides only 5GB for video recording. Also, apps can be developed to perform all postprocessing analysis of the videos taken on the smartphone. Using the videos taken with the smartphone, the distribution of cell sizes derived from ~100 cells for each cell line are shown in Figure 1 adjacent to the images of the cell monolayers. MDA-MB-231 (Figure 1a) cells exhibit a biphasic size distribution with peaks at 13 and 16 μm. HCC-1806 (Figure 1b), MCF-7 (Figure 1c), and MCF-10A (Figure 1d) cells have monophasic size distributions with peaks at 13, 15, and 16 μm, respectively.

Multiconstriction Channel Array Microfluidic Chip.—The microfluidic device contains two rows of multiconstriction channels, named sequential deformation channel (SDC) 1 and 2, referred to as SDC1 and SDC2 in Figure 2a, respectively. Each row has six identical multiconstriction channels with four constriction regions (width, 8 μm height, 8 μm; length, 50 μm) and three relaxation regions (width, 25 μm; height, 30 μm; length, 25 μm). A transition channel (TC) (center channel in blue, vertical to the multiconstriction channels) between SDC1 and SDC2 is created to function as a buffer for maintaining the constant pressure before the cells enter the SDC2. In addition, the width of 100 μm in the center channel allows the cells to relax longer and possibly recover to their original spherical shape before entering SDC2. It is noteworthy that, in this chip, we have separated the sensing channels and the delivery channel. This will minimize the possibility of channel clogging at the introduction of cells. We also treated the microchannel with EDTA before experiment for 30 min to reduce the chance of cells being stuck in the constriction channel. However, clogging may still be happening due to the small microchannel dimensions and the presence of larger and stiffer particles. We used 30 μm filters during the sample preparation.

When large particles go inside the channel and disturb the flow, we reverse the negative pressure to push the large particles/cells back to the delivery channel, whose flow was kept constant during this procedure. We performed this operation as needed (not more than once per minute). We had six parallel channels and we did not have clogging on all channels. So, practically, we did not have to do this until all channels are clogged. The reason we did this though was to ensure that the videos and subsequent data analysis are being carried out while all channels are performing as normal and no very large particles have obstructed the flow. There are ways to address this in the future: by making more channels in parallel, using a finer filter, using a filter array as part of the chip to prevent the large particles from flowing, and even programming the pressure pump to reverse the pressure automatically for any possible clogging.

Incremental Velocity Profiles of Breast Cell Lines.—Single cell suspensions were introduced to the delivery channel and the transit of individual cells through SDC1 and SDC2 were monitored by video imaging. In the case of both cell lines and patient samples, ~45–50% of the cells were passing through SDC1 and SDC2. Other cells were flowing along the delivery channel into the cell waste outlet. The data were collected from the videos of cells passing through the channels under a constant pressure. If a large particle/cell was clogging any part of SDC1 or SDC2, the data from that cell will not be used in data analysis. Transit velocities were measured from the videos. To gain greater resolution in the velocity profile, we obtained two velocity measurements in each constriction segment (Figure 2b). For example, in SDC1, the transit velocity through the initial constriction segment was designated 1 and 2. The velocities in segments 1–16 were recorded as v_1, v_2, …, v_{16}, respectively. The velocity increments between two different sections were defined as

$$\alpha_{m,n} = (v_m - v_n)/v_n \, (m = 1, 2, \ldots, 16; \;\; n = 1, 2, \;\; \ldots, 16) \tag{1}$$

where m and n were the sequence number to identify the velocities. It is noteworthy that our chip can provide other information including aspect ratio of each cell after going through SDC1 and SDC2 as well as the deformed length of each cell at each section of SDCs. However, collection of these data requires heavy image processing which is beyond the scope of this work. We only analyzed and included the velocity profiles as biomechanical properties as a simpler and faster technique. We can envision, however, that in future, by establishing automated image processing algorithms for more complex video analysis, we can include data from other parameters in our machine learning system.

The experiments on each cell line were repeated on more than three devices to prove the repeatability and reliability of this device. The velocity results of the three malignant cell lines, illustrated in Figure 2b, all showed a characteristic profile in which the transit velocities through successive constriction segments in SDC1increase, then this repeats as cells enter SDC2. The nontumorigenic MCF-10A cells do not follow this pattern. The entry velocities of MDA-MB-231 (segment 1 in red) and HCC-1806 (segment 1 in pink) in SDC1 are higher than the entry velocities of MCF-7 (segment 1 in orange) and MCF-10A (segment 1 in blue). The initial velocities of the MDA-MB-231 and HCC-1806 are 457 ± 598 μm/s (n = 96) and 376 ± 242 μm/s (n = 108), respectively. The velocity profiles at population level and the trends of the velocity variations of MDA-MB-231 and HCC-1806 are similar. The

variations of velocities are related to cells' dynamic biomechanical properties which are functions of cells' cytoskeletal architecture, cell size, cell morphology and surface roughness, and possibly the mitosis cell cycles.[13,29–34] The microfluidic channels were treated with EDTA to minimize the cell stickiness to the surface of PDMS channel. The cell adhesion is an important component of the properties of the cells; however, the cell will not adhere to channel surface in the short time of cells passing through the microchannels. The cell requires a much longer time to adhere to the channel wall. The velocity profile reveals the biomechanical properties of the cell stiffness and cytoskeleton strength. To analyze the different cell lines by velocity profiles, we used the kernel-based machine learning method to find the variables that represents the biomechanical properties of different cell lines. After passing through the SDC1, the cancer cell lines MDA-MB-231, HCC-1806, and MCF-7 show a higher entry velocity in SDC2 (segment 9 in red, pink, and orange, respectively) than MCF-10A (segment 9 in blue). Based on the *t* test results of velocities at segment 9, the velocity of MDA-MB-231 being higher than that of MCF-10A has a $t = 11.1$, $p < 0.0001$; even assuming the velocity of MDA-MB-231 being three times higher than that of MCF-10A has a $t = 2.132$, $p = 0.017$. The velocity of HCC-1806 being higher than that of MCF-10A has a $t = 12.1$, $p < 0.0001$; assuming the velocity of HCC-1806 twice higher than that of MCF-10A has a $t = 3.65$, $p = 0.0002$. The velocity of MCF-7 higher than than that of MCF-10A has a $t = 11.5$, $p < 0.0001$; assuming the velocity of MCF-7 2.5 times higher than that of MCF-10A has a $t = 2.37$, $p = 0.009$.

The cancer cell line MDA-MB-231 deformed faster at the segment 2 of SDC1. After passing through SDC1, the MDA-MB-231 cells are recovered back to spherical geometry and become easier to deform at the entrance (segment 9) of SDC2. The normal cell line MCF-10A cells experience a different passing procedure. MCF-10A cells, which are stiffer than cancer cells,[15,31–33,35–38] require a longer deformation time at the segment 1 of SDC1. After passing through SDC1, the MCF-10A cells are not fully recovered back to spherical structure, which, due to cell rotation in TC, can result in a longer time to deform again and move into the entrance of SDC2 (segment 9). (Additional images available in Supporting Information Figure S1). However, when they deform completely and get into SDC2, their transit is generally slower compared to their velocities in SDC1. As illustrated in Figure 2b, the average velocity of MCF-10A in SDC2 (segments 9–16 in blue) is lower than those of the three cancer cell lines. The three cancer cell lines show similar velocity profiles in SDC2 (segments 9–16 in red, pink, and orange) and SDC1.

The multiconstriction microfluidic device improves the resolution in distinguishing cancer cells from normal cells compared with single constriction channel microfluidic devices.[3,37,39,40] The two rows of channels create 16 velocity segments in constriction regions for data analysis, which yields 120 variables using the definition in eq 1. We select eight velocity increments at the same segments of SDC1and SDC2 as variables:

$$\begin{cases} \alpha_{16,08} = (v_{16} - v_{08})/v_{08} \\ \alpha_{15,07} = (v_{15} - v_{07})/v_{07} \\ \alpha_{14,06} = (v_{14} - v_{06})/v_{06} \\ \alpha_{13,05} = (v_{13} - v_{05})/v_{05} \\ \alpha_{12,04} = (v_{12} - v_{04})/v_{04} \\ \alpha_{11,03} = (v_{11} - v_{03})/v_{03} \\ \alpha_{10,02} = (v_{10} - v_{02})/v_{02} \\ \alpha_{09,01} = (v_{09} - v_{01})/v_{01} \end{cases} \quad (2)$$

Together with the size information, 16 velocity segments, and eight additional velocity increments defined by eq 1, we can analyze 25 variables by three methods, Ridge,[24] NGK,[26] and Lasso.[25] The kernel-based machine learning algorithm can be applied on a group of cells with limited sample size. The key is to extract sufficient quantity of variables, which can be considered as high-dimensional variables combinations.[26,41]

Consider n observations for each cell type t, $t = 1, \ldots, T$, and p variables data set (y, X_t), where $X_t = [x_{1t}, x_{2t}, \ldots, x_{pt}]$, $x_{jt} = [x_{j1t}, x_{j2t}, \ldots, x_{jnt}]^T$ is an $n \times 1$ vector for the jth variable, $j = 1, \ldots, p$. Ridge and Lasso conduct variable selections based on the following generalized linear model for multinomial response,

$$\Pr(y = t | X_t) = H(\beta_0 + \beta_1 x_{1t} + \ldots + \beta_p x_{pt}) \quad (3)$$

where $H(\cdot)$ is a logit function and

$$\sum_{t=1}^{T} \Pr(y = t | X_t) = 1 \quad (4)$$

Ridge and Lasso conduct variable selection using L2 norm $\|\beta\|^2$ and using L1 norm $\|\beta\|$, respectively, where $\beta = (\beta_0, \beta_1 \ldots, \beta_p)^T$ Ridge's objective function is to minimize the following objective function,

$$\log\left[\prod_{t=1}^{T} \Pr(y = t | X_t)^t\right] + \lambda \left\|\beta\right\|^2 \quad (5)$$

while Lasso is to minimize the following objective function

$$\log\left[\prod_{t=1}^{T} \Pr(y = t | X_t)^t\right] + \lambda \left\|\beta\right\| \quad (6)$$

However, NGK performed variable selection using non-parametric and nonlinear model using kernel function. According to the Representer theorem, the nonparametric regression model can be expressed as

$$\Pr\left(y = t \middle| X_t\right) = H\left[f\left(X_t\right)\right] = H(K\alpha) \tag{7}$$

where $f(X_t)$ is the unknown nonparametric function, K is the kernel matrix corresponding to the function Hilbert space, and α is unknown parameter. Our kernel can be expressed in a nonlinear function form because the Gram matrix

$$K\left(\xi, X_t\right) = g\left(\sum_{j=1}^{p} \xi_j D^j\right) \tag{8}$$

where g is a known function (i.e., Gaussian form), D^j is the matrix with (k,l)th entry $d_{kl}^j = -\left(x_{jk} - x_{jl}\right)^2$. We performed variable selection using $\xi = (\xi_0, \xi_1, \ldots, \xi_p)$. The objective function for NGK is to conduct the variable selection for minimizing the objective function,

$$\log\left[\prod_{t=1}^{T} \mathrm{H}\{K\alpha(\xi)\}^t\right] + \lambda\left\|\xi\right\| \tag{9}$$

The prediction accuracy is calculated using 10-fold cross-validations (CV). This means that we have 10 training and 10 test data sets. Using a given training set, we perform variable selections. We then build the classifier and calculate the prediction accuracy using the test set. This procedure is repeated 10 times. The probability of correctly predicting the test group is named as the prediction value. Then, we are able to find the prediction value to distinguish between two different groups, either cell lines or patient samples. The full table of prediction values of different combinations of the selected variables is available in Supporting Information.

One test of our approach is its reliability in distinguishing malignant and nonmalignant breast cell lines. The prediction values (Figure 3) calculated by the Ridge, NGK, and Lasso methods show how well individual cell lines are distinguished based on their cell size and incremental transit velocities. All three statistical methods distinguished the malignant cell lines from the immortalized MCF-10A line with prediction values of 0.80–0.85 (Figure 3a).

Next individual malignant cell lines are compared. Here, there are some interesting observations. The two TNBC cell lines (MDA-MB-231 and HCC-1806) which are both metastatic in nude mice[42] exhibited differential biomechanical properties with predictive values between 0.65 and 0.7; thus even though both are TNBC, there is modest confidence (65–70%) to distinguish between them (Figure 3b). The differences between breast cancer cell lines MDA-MB-231 and MCF-7 have been studied form both biochemical and biophysical[43–45] points. The biophysical differences were studied by impedance spectroscopy that focuses on the specific membrane capacitance and cytoplasm conductivity.[2,27,46] Surprising at first, there is even less confidence (between 0.6 and 0.65) in the ability to distinguish the MDA-MB-231 from the MCF-7 cell line which is not metastatic in nude

mice[47] (Figure 3c). However, the Lasso method distinguished the HCC-1806 and MCF-7 cell lines with a high predictive value of 0.8 (Figure 3c). We conclude that the results in Figure 3b and c are more consistent with the patient origins of each of these cell lines rather than their metastatic behavior in nude mice or their hormone receptor status. This makes our multiconstriction channel approach unique, possibly more representative of metastatic risk in patients. By way of explanation, the HCC-1806 cell line is derived from a patient with a nonmetastatic primary tumor classified as a grade II acantholytic squamous carcinoma of the breast (ATCC) with basal B characteristics.[42] In contrast, both the basal B TNBC MDA-MB-231 cell line and the hormone-responsive ductal adenocarcinoma line MCF-7 are derived from the pleural effusions of patients with metastatic breast cancer (ATCC). Thus, our approach might key on an as yet unidentified mechanical property characteristic of the metastatic, pleural effusion origin of MDA-MB-231 and MCF-7 cells. In support of this idea, even though studies have shown MCF-7 cells have a stiffer cytoskeleton structure with a higher Young's modulus,[7,48] others reported single constriction channel devices has limited capability in differentiating between MDA-MB-231 and MCF-7.[49]

Cell Recovery from Human Breast Biopsies.

From patients undergoing partial or complete mastectomy, cancer cells (CA) and adjacent normal cells (NR) were collected separately and prepared identically by a method to enrich epithelial organoids. Slides were prepared from each single cell suspension; epithelial cells (pancytokeratin+), lymphoid cells (CD45+), macrophages plus and histiocytes (CD68+) were enumerated after immunohistochemical (IHC). Slides were then stained with H&E. Representative images were shown in Figure 4(a–d). In the cancer samples, epithelial cells were cancer (CA) while in the adjacent normal samples, the epithelial cells were normal (NR) as assessed by a pathologist.

The nuclear-cytoplasmic ratio (N/C ratio) of normal epithelial cells is 1:4–1:6, while the N/C ratio of malignant carcinoma cells can reach 2:1. The epithelial cells in cancer samples show a larger nucleus in dark color. The large epithelial cells with hyperchromasia and increased N/C ratio represent carcinoma cells in patient A and patient B. Differential cell counts estimated the percentage of epithelial cells, lymphoid cells, and macrophage/histiocytes (M/H) in each of the patient samples. Individual cell sizes by cell type are measured in 1000× images. The average size of epithelial, lymphoid and M/H populations in each of the patient samples is presented in Table 1.

Incremental Velocity Profile Analysis of Primary Human Tissue Samples.

Cell suspensions were passed through 30 μm filter screens to remove large cell clusters prior to velocity testing. The patient A, CA sample contained ~2.5×10^4 cells/mL; the patient A NR contained ~0.5×10^4 cells/mL. The patient B, CA sample was ~2.5×10^4 cells/mL; the patient B NR sample was ~1.5×10^4 cells/mL. The total number of cells in each velocity analysis is indicated by "n" in Figure 4e.

The velocity profile of CA and NR from both patient samples (Figure 4) exhibited the same incremental velocity profile as observed for the cell lines (Figure 2b). There was progressive increase in velocity with each segment in the first channel and then a repeat of this pattern in

the second channel. These data largely reflect the epithelial cells in each sample. The small mature lymphocytes had a cell size around 8–10 μm, which was smaller than the dimensions of constriction channels. Without deformation in the constriction channels, the lymphocytes passed through all channels at the flow velocity of the medium.

The Lasso analysis yields the highest predictive value in discriminating CA and NR cells from patient samples (Figure 5). For patient A, CA and NR cells show a prediction value of 0.79 which approaches that achievable in the cell lines. The CA and NR cells from patient B show a less robust prediction value of 0.7. These results are obtained using patient biopsies that received minimal processing in order to retain all elements of tumor heterogeneity within the sample provided. We suggest that this high content microfluidic approach coupled with kernel based learning analysis has promise for distinguishing patient-derived cancer cells in small biopsy samples with less than a 24 h assay turn-around time. The Lasso analysis also indicates that the two patient CA samples are more similar to each other (prediction value 0.6) than either CA compared to its patient-matched NR sample. This is of interest considering that patient A and B have undergone different therapeutic regimens prior to biopsy. Patient A has both chemotherapy and radiation therapy, while patient B does not receive any therapy. This suggests that prior treatment may not interfere with the ability of this microfluidic approach to identify cancer cells in patient biopsies. There is no gold standard for applying prediction values for clinical cancer diagnosis. Our results indicate that this device can be used in patient samples to reach a quantitatively comparison for clinical samples other than standard image reading in IHC studies.

DISCUSSION

The evaluation of the risk of tumor recurrence and metastasis, and localized tumor infiltration status of breast cancer is a challenge. Typically, IHC technology is used in cancer diagnosis today to assess tumor grade and local infiltration status. These well-established IHC protocols are expensive, time-consuming and labor intensive, and still cannot definitively assess metastatic or recurrence risk in every patient.[50–52] With the assistance of machine learning methods, the analysis of IHC studies can be improved.[53] Genetic screens are available for predicting cancer recurrence but are not widely available to all patients.[54,55] One confounding factor in diagnosing risk is the heterogeneous nature of cells within patient biopsy samples.[56] As reviewed by Marjanovic et al., patient mastectomy samples collected at surgery usually contain a heterogeneous mixture of both cancerous and normal cells. When adjacent normal samples are dissociated into single cell suspensions, proliferating cancer cells are also seen.[56] Consequently, adjacent normal tissue is not commonly regarded as completely normal due to admixture with infiltrating cancerous cells. Here we demonstrated using heterogeneous patient breast tumor and normal tissue samples and a high-throughput microfluidic channel array device, cell biomechanical properties can be recorded at a rate of over 500 cells in 10 min with an inexpensive disposable microchip. In addition, we only analyzed ~45–50% of the cells passing through SDC1 and SDC2. This can also contribute to a reduction in prediction rate especially in patient samples containing a heterogeneous population of cells. Recycling the unanalyzed portion of the sample and performing the microfluidic analysis on those cells can enhance the prediction accuracy of our assay. The smartphone slow motion video can record sufficient velocity information as a

replacement of expensive high-speed camera. This approach indicates that our device and method has a promising potential to be utilized in clinical applications with the development of smartphone technologies. Cell transit velocity data analysis using kernel learning-based statistical analysis identifies normal and tumor cells in very small biopsy samples based upon their biophysical traits which can augment current clinical diagnostic assessments.

Microfluidic technologies to study cancer cells have been carried out with a multitude of microfluidic platforms.[5,6,11,46,57] Single constriction channel technology with added impedance spectroscopy has shown promise in distinguishing between cancerous and normal cells from multiple cell lines.[4,49,58,59] However, characterization and separation of different subtypes of cancer cell lines are still challenging by microfluidic single constriction channel with impedance spectroscopy.[6,7,60] Single channel designs with multiconstriction regions were found to amplify the biomechanical differences between breast cancer cell lines and nontumorigenic breast epithelial cell lines. The studies of channels with five constriction regions showed differentiation between breast cancer cell line MDA-MB-231 and normal cell line MCF-10A could be achieved with 95% accuracy.[3] Cells entering the constriction channel undergo dynamic cell deformation changes. Analysis of the constriction channel entry velocity versus the constriction channel exit velocity indicate that cells of the nontumorigenic breast cell line has difficulty recovering from their deformed elliptical shape to their original spherical geometry. This differential recovery of shape plays a key role in differentiating the tumorigenic and nontumorigenic breast cell lines. To scale up throughput toward use of this design in clinical applications, here we test a microchip design with parallel channels containing four constriction regions each. Combining the machine learning technology has attracted the attention of the lab-on-a-chip community on cell research. Starting from the American Association of Cancer Research (AACR) annual meeting 2017 in Washington, DC.,[61–63] the application of artificial intelligence and machine learning gained more progress in cancer research. Many approaches were made by involving many different machine learning algorithms in their cancer research.[64–66] Nyberg et al. presented a cancer invasion study by k-nearest neighbor machine learning algorithm in 2018.[67] The Nyberg et al.[67] paper is based on short constriction channels they developed with Rowat's group.[68,69] They developed their multiple constriction channels to detect the deformation parameters of different cell lines. The constriction channel they presented were short, which did not cause the full deformation of the single cells. As presented in Nyberg et al.,[67] they studied the cell invasion by performing k-nearst neighbor (kNN) machine learning on six parameters from the multiple short constriction channels. The short constriction channel can collect the dynamic motions of the cell deformation as a model to study invasiveness. The Rowat paper, in fact, is a good method of using multi-parametric single cell analysis for predicting cell invasion behavior. Both their work and our work are a testimony that not just a single parameter but a collection of physical attributes are powerful to differentiate cells and to predict their disease status. Our work is different from that of Rowat et al. in that we use multiconstriction structures and collect different biophysical parameters when compared to Rowat et al. Rowat et al. use a single transition channel and then utilizes parameters such as size, elastic modulus, transit time, and maximum strain (some of these parameters are not directly measured by the microfluidic channel with kNN method to achieve 94–100% identification rate of 5 cell lines. The Rowat paper extracted elastic modulus and cell fluidity

parameters by preselecting the cell size population median ±1 μm. In our work, we considered all cells sizes from 11 to 21 μm to guarantee the heterogeneity of the sample we used. The size distribution is presented in Figure 1. If we only analyze the cells by size median ±1 μm, we will lose 51.0% of the MDA-MB-231 cells, 33.3% of the HCC-1806 cells, 43.6% of the MCF-7 cells, and 42.3% of the MCF-10A cells. The elastic modules and cell fluidity parameter collection in the Rowat paper requires post calculation and data fitting a rheology model with time dependent strain data. On the contrary, we can harvest parameters directly from velocity profiles to minimize the work load of data post processing. Consistent with our previous work,[1,70] we used our longer constriction channels to allow the cells to fully deform and transit through the channel, which is another model to study the tumor metastasis by biomechanical properties. The short channel in the work of Rowat et al. can only provide two time variables: entry time and transit time. Based on their kNN method, the time variables provided 0.33–0.86 positive rates. Our multiconstriction channels provided more time variables. Together with kernel method, we can reach 81–85% prediction values. Our approach does not require the calculation of other biophysical parameters from the cells, which demonstrated an easier way to analyze dynamic motions of the cells. The Rowat paper concluded that a more sophisticated machine learning method can further improve the performance of study invasiveness. Our kernel-based algorithm is a significant improvement of the machine learning approach. It is also notable that the kNN classifiers used in Nyberg et al.[67] are memory-based and require no model fit. This kNN approach is a nonparametric algorithm that does not assume the underlying data fits a particular model. It is a machine learning tool. The class assigned to new data points is determined by the most common class of the k number of nearest neighbors in the training set. These neighbors are determined using Euclidean distance. Hence this approach depends on the selection of k and distance measure; our NGK does not. Our NGK classifier is a nonparametric kernel machine based approach. Our NGK is not memory-based. We can consider NGK is a hybrid approach which is a mixed of nonparametric model and kernel machine tool. Using a training set, we built NGK classifier which is required to estimate nonparametric function but does not assume the particular function form. This nonparametric function is estimated via Gaussian process, which is known as a family of nonparametric functions. Unlike kNN, the class assigned to new data points is determined by the probability that new point is assigned to the certain class.

The TNBC MDA-MB-231 is representative of a highly invasive, rapidly proliferating basal breast malignancy expressing markers of cells, including P-cadherin and/or cadherin-11.[71,72] Both P-cadherin and cadherin-11 promote motility and invasiveness.[73] The MCF-7 cell line is a model of endocrine therapy responsive luminal A breast cancer expressing both ER and progesterone (PR) receptors and also differentiation markers more typical of its epithelial cell origin such as E-cadherin[74] which is associated with lower motility and lower invasiveness. MDA-MB-231 express vimentin which makes them more mesenchymal in nature than HCC-1806 which exhibit a more vimentin.[75]

The TNBC cell lines MDA-MB-231 and HCC-1806 show similar velocity profiles in the high-throughput microfluidic channel array. The first deformation and secondary deformation indicate that both cells have similar deformation and transition times. The similar recovery ability to their original spherical shape indicates that both cells have similar

biomechanical properties, such as cell membrane and cytoskeleton elasticity. The comparison of these two cell lines by the high-dimensional variables analysis of Ridge, NGK, and Lasso indicates that there are still differences between the two cell lines. Since all cells are breast cells, interactions among these variables within the same cell type and interactions between different cell types are not expressed as parametric models. The performance between Lasso and NGK is similar which means that the model for the data is more likely parametric model. NGK provides flexibility for both additive and nonadditive nonparametric models and it also provides flexibility for both parametric and nonparametric modeling. This kernel-based classifier is developed by connecting a kernel machine with the multivariate nonparametric regression model. This approach can simultaneously perform a variable selection in nonadditive multivariate nonparametric model for analyzing high-dimensional large data. Using NGK, we nonparametrically model unknown interaction terms among high dimensional variables. Especially in patient primary tumor samples, the heterogeneous status may include more nonlinear relationships among all the velocity-related variables we established.

The heterogeneous character of human tumors is commonly accepted.[76] We are able to distinguish cells isolated from biopsies of tumors and adjacent normal tissue based solely on their biomechanical properties with a prediction rate of 70.07%–75.96% considering that we processed only 50% of each sample. Therefore, in tests of two patients, the prediction rate, i.e., the ability to accurately identify a cell as tumor or normal, was 5–10% less than that achieved with the cell lines. Considering the greater heterogeneity of the patient samples, this result is quite strong. Of note is the observation that the tumor cells removed from the patient A whose primary tumor has already metastasized concludes a higher prediction value than patient B with the nonmetastatic tumor when compared to adjacent normal tissue. Clearly, the multiconstriction microfluidic channel is not a stand-alone assay for patient risk assessment at this point; many more patient samples need to be analyzed. Significantly, our patient population is primarily African American. As has been documented repeatedly, African Americans have much higher breast cancer mortality rates than Caucasian patients, and a substantial component lies in as yet unidentified differences in cancer biology;[77–79] thus, a biomechanical diagnostic test might prove particularly of benefit to this patient population.

Supplementary Material

Refer to Web version on PubMed Central for supplementary material.

ACKNOWLEDGMENTS

The authors would like to thank National Institute of Health (NIH) National Cancer Institute R21CA210216 and National Science Foundation (NSF) CBET-1403304, and Charles and Mary Latham Fund for supporting this research project. The authors acknowledge the Micro & Nano Fabrication Laboratory at Virginia Tech for the equipment support.

ABBREVIATIONS

NGK	nonnegative garrote on kernel machine

DCIS	ductal carcinoma in situ
EMT	epithelial-mesenchymal transition
AFM	atomic force microscopy
FBS	fetal bovine serum
EGF	epidermal growth factor
PDMS	polydimethylsiloxane
TNBC	triple-negative breast cancer
SDC	sequential deformation channel
TC	transition channel
IHC	immunohistochemical
N/C	nuclear-to-cytoplasmic
M/H	macrophage/histiocytes
kNN	k-nearest neighbor

REFERENCES

(1). Babahosseini H; Strobl JS; Agah M Microfluidic iterative mechanical characteristics (iMECH) analyzer for single-cell metastatic identification. Anal. Methods 2017, 9 (5), 847–855. [PubMed: 29034007]

(2). Babahosseini H; Strobl JS; Agah M Single cell metastatic phenotyping using pulsed nanomechanical indentations. Nanotechnology 2015, 26 (35), 354004. [PubMed: 26266760]

(3). Ren X; Ghassemi P; Babahosseini H; Strobl J; Agah M Single-Cell Mechanical Characteristics Analyzed by Multi-Constriction Microfluidic Channels. ACS Sensors 2017, 2 (2), 290–299. [PubMed: 28723132]

(4). Chen J; Xue C; Zhao Y; Chen D; Wu M-H; Wang J Microfluidic impedance flow cytometry enabling high-throughput single-cell electrical property characterization. Int. J. Mol. Sci 2015, 16 (5), 9804–9830. [PubMed: 25938973]

(5). Xue C; Wang J; Zhao Y; Chen D; Yue W; Chen J Constriction channel based single-cell mechanical property characterization. Micromachines 2015, 6 (11), 1794–1804.

(6). Chen J; Li J; Sun Y Microfluidic approaches for cancer cell detection, characterization, and separation. Lab Chip 2012, 12 (10), 1753–1767. [PubMed: 22437479]

(7). Hu S; Lam RH Characterization of viscoelastic properties of normal and cancerous human breast cells using a confining microchannel. Microfluid. Nanofluid 2017, 21 (4), 68.

(8). TruongVo T; Kennedy R; Chen H; Chen A; Berndt A; Agarwal M; Zhu L; Nakshatri H; Wallace J; Na S; et al. Microfluidic channel for characterizing normal and breast cancer cells. J. Micromech. Microeng 2017, 27 (3), 035017.

(9). Siravegna G; Marsoni S; Siena S; Bardelli A Integrating liquid biopsies into the management of cancer. Nat. Rev. Clin. Oncol 2017, 14 (9), 531. [PubMed: 28252003]

(10). Hegemann M; Stenzl A; Bedke J; Chi KN; Black PC; Todenhöfer T Liquid biopsy: ready to guide therapy in advanced prostate cancer? Bju international 2016, 118 (6), 855–863. [PubMed: 27430478]

(11). Babahosseini H; Strobl JS; Agah M Microfluidic Iterative Mechanical Characteristics (iMECH) Analyzer for Single-Cell Metastatic Identification. Anal. Methods 2017, 9 (5), 847–855. [PubMed: 29034007]

(12). Luo Y; Chen D; Zhao Y; Wei C; Zhao X; Yue W; Long R; Wang J; Chen J A constriction channel based microfluidic system enabling continuous characterization of cellular instantaneous Young's modulus. Sens. Actuators$_y$ B 2014, 202, 1183–1189.

(13). Babahosseini H; Carmichael B; Strobl J; Mahmoodi S; Agah M Sub-cellular force microscopy in single normal and cancer cells. Biochem. Biophys. Res. Commun 2015, 463 (4), 587–592. [PubMed: 26036579]

(14). Corbin EA; Kong F; Lim CT; King WP; Bashir R Biophysical properties of human breast cancer cells measured using silicon MEMS resonators and atomic force microscopy. Lab Chip 2015, 15 (3), 839–847. [PubMed: 25473785]

(15). Cross SE; Jin Y-S; Rao J; Gimzewski JK Nanomechanical analysis of cells from cancer patients. Nat. Nanotechnol 2007, 2 (12), 780–783. [PubMed: 18654431]

(16). Lekka M; Laidler P; Gil D; Lekki J; Stachura Z; Hrynkiewicz A Elasticity of normal and cancerous human bladder cells studied by scanning force microscopy. Eur. Biophys. J 1999, 28 (4), 312–316. [PubMed: 10394623]

(17). Rosenbluth MJ; Lam WA; Fletcher DA Force microscopy of nonadherent cells: a comparison of leukemia cell deformability. Biophys. J 2006, 90 (8), 2994–3003. [PubMed: 16443660]

(18). Hochmuth R M. Micropipette aspiration of living cells. J. Biomech 2000, 33 (1), 15–22. [PubMed: 10609514]

(19). Hoffman RM Imaging the role of the tumor microenvironment in tumor progression and metastasis. Cancer Cell Microenviron. 2016, 3 (2), e1206.

(20). Lee GY; Lim CT Biomechanics approaches to studying human diseases. Trends Biotechnol. 2007, 25 (3), 111–118. [PubMed: 17257698]

(21). Guck J; Schinkinger S; Lincoln B; Wottawah F; Ebert S; Romeyke M; Lenz D; Erickson HM; Ananthakrishnan R; Mitchell D; et al. Optical deformability as an inherent cell marker for testing malignant transformation and metastatic competence. Biophys. J 2005, 88 (5), 3689–3698. [PubMed: 15722433]

(22). Suresh S; Spatz J; Mills J; Micoulet A; Dao M; Lim C; Beil M; Seufferlein T Reprint of: connections between single-cell biomechanics and human disease states: gastrointestinal cancer and malaria. Acta Biomater. 2015, 23, S3–S15. [PubMed: 26235344]

(23). Wang N; Ingber DE Probing transmembrane mechanical coupling and cytomechanics using magnetic twisting cytometry. Biochem. Cell Biol 1995, 73 (7–8), 327–335. [PubMed: 8703406]

(24). Hoerl AE; Kennard RW Ridge regression: Biased estimation for nonorthogonal problems. Technometrics 1970, 12 (1), 55–67.

(25). Tibshirani R Regression shrinkage and selection via the lasso. J. R. Stat. Soc. B 2011, 73, 273–282.

(26). Fang Z; Kim I; Schaumont P Flexible variable selection for recovering sparsity in nonadditive nonparametric models. Biometrics 2016, 72 (4), 1155–1163. [PubMed: 27077330]

(27). Babahosseini H; Srinivasaraghavan V; Zhao Z; Gillam F; Childress E; Strobl JS; Santos WL; Zhang C; Agah M The impact of sphingosine kinase inhibitor-loaded nanoparticles on bioelectrical and biomechanical properties of cancer cells. Lab Chip 2016, 16 (1), 188–198. [PubMed: 26607223]

(28). Babahosseini H; Strobl JS; Agah M Using nanotechnology and microfluidics in search of cell biomechanical cues for cancer progression. Nanomedicine 2015, 10 (17), 2635–2638. [PubMed: 26328619]

(29). Babahosseini H; Roberts PC; Schmelz EM; Agah M Bioactive sphingolipid metabolites modulate ovarian cancer cell structural mechanics. Integrative Biology 2013, 5 (11), 1385–1392. [PubMed: 24056950]

(30). Nikkhah M; Strobl JS; Agah M Attachment and response of human fibroblast and breast cancer cells to three dimensional silicon microstructures of different geometries. Biomed. Microdevices 2009, 11 (2), 429. [PubMed: 19058013]

(31). Nikkhah M; Strobl JS; De Vita R; Agah M The cytoskeletal organization of breast carcinoma and fibroblast cells inside three dimensional (3-D) isotropic silicon microstructures. Biomaterials 2010, 31 (16), 4552–4561. [PubMed: 20207413]

(32). Nikkhah M; Strobl JS; Peddi B; Agah M Cytoskeletal role in differential adhesion patterns of normal fibroblasts and breast cancer cells inside silicon microenvironments. Biomed. Microdevices 2009, 11 (3), 585. [PubMed: 19089620]

(33). Nikkhah M; Strobl JS; Schmelz EM; Roberts PC; Zhou H; Agah M MCF10A and MDA-MB-231 human breast basal epithelial cell co-culture in silicon micro-arrays. Biomaterials 2011, 32 (30), 7625–7632. [PubMed: 21764441]

(34). Nikkhah M; Strobl JS; Srinivasaraghavan V; Agah M Isotropically etched silicon microarrays for rapid breast cancer cell capture. IEEE Sens. J 2013, 13 (3), 1125–1132.

(35). Xu W; Mezencev R; Kim B; Wang L; McDonald J; Sulchek T Cell stiffness is a biomarker of the metastatic potential of ovarian cancer cells. PLoS One 2012, 7 (10), e46609. [PubMed: 23056368]

(36). Swaminathan V; Mythreye K; O'Brien ET; Berchuck A; Blobe GC; Superfine R Mechanical stiffness grades metastatic potential in patient tumor cells and in cancer cell lines. Cancer Res. 2011, 71 (15), 5075–5080. [PubMed: 21642375]

(37). Hou HW; Li Q; Lee G; Kumar A; Ong C; Lim CT Deformability study of breast cancer cells using microfluidics. Biomed. Microdevices 2009, 11 (3), 557–564. [PubMed: 19082733]

(38). Agus DB; Alexander JF; Arap W; Ashili S; Aslan JE; Austin RH; Backman V; Bethel KJ; Bonneau R; Chen W-C A physical sciences network characterization of non-tumorigenic and metastatic cells. Sci. Rep 2013, 3, 1449. [PubMed: 23618955]

(39). Adamo A; Sharei A; Adamo L; Lee B; Mao S; Jensen KF Microfluidics-based assessment of cell deformability. Anal. Chem 2012, 84 (15), 6438–6443. [PubMed: 22746217]

(40). Guan G; Chen PC; Peng WK; Bhagat AA; Ong CJ; Han J Real-time control of a microfluidic channel for size-independent deformability cytometry. J. Micromech. Microeng 2012, 22 (10), 105037.

(41). Fang Z; Kim I Bayesian Ising Graphical Model for Variable Selection. Journal of Computational and Graphical Statistics 2016, 25 (2), 589–605.

(42). Volk-Draper LD; Rajput S; Hall KL; Wilber A; Rana S Novel model for basaloid triple-negative breast cancer: behavior in vivo and response to therapy. Neoplasia 2012, 14 (10), 926–942. [PubMed: 23097627]

(43). Zheng Y; Nguyen J; Wei Y; Sun Y Recent advances in microfluidic techniques for single-cell biophysical characterization. Lab Chip 2013, 13 (13), 2464–2483. [PubMed: 23681312]

(44). Song H; Wang Y; Rosano JM; Prabhakarpandian B; Garson C; Pant K; Lai E A microfluidic impedance flow cytometer for identification of differentiation state of stem cells. Lab Chip 2013, 13 (12), 2300–2310. [PubMed: 23636706]

(45). Berezin MY; Achilefu S Fluorescence lifetime measurements and biological imaging. Chem. Rev 2010, 110 (5), 2641–2684. [PubMed: 20356094]

(46). Chen J; Zheng Y; Tan Q; Shojaei-Baghini E; Zhang YL; Li J; Prasad P; You L; Wu XY; Sun Y Classification of cell types using a microfluidic device for mechanical and electrical measurement on single cells. Lab Chip 2011, 11 (18), 3174–3181. [PubMed: 21826361]

(47). Shafie SM; Liotta LA Formation of metastasis by human breast carcinoma cells (MCF-7) in nude mice. Cancer Lett. 1980, 11 (2), 81–87. [PubMed: 6450636]

(48). Dokukin ME; Guz NV; Sokolov I Mechanical properties of cancer cells depend on number of passages: Atomic force microscopy indentation study. Jpn. J. Appl. Phys 2017, 56 (8S1), 08LB01.

(49). Han A; Yang L; Frazier AB Quantification of the heterogeneity in breast cancer cell lines using whole-cell impedance spectroscopy. Clin. Cancer Res 2007, 13 (1), 139–143. [PubMed: 17200348]

(50). Ihemelandu CU; Leffall LD; Dewitty RL; Naab TJ; Mezghebe HM; Makambi KH; Adams-Campbell L; Frederick WA Molecular breast cancer subtypes in premenopausal and postmenopausal African-American women: age-specific prevalence and survival. J. Surg. Res 2007, 143 (1), 109–118. [PubMed: 17950079]

(51). Canas-Marques R; Schnitt SJ E-cadherin immunohisto-chemistry in breast pathology: uses and pitfalls. Histopathology 2016, 68 (1), 57–69. [PubMed: 26768029]

(52). Vrekoussis T; Chaniotis V; Navrozoglou I; Dousias V; Pavlakis K; Stathopoulos E; Zoras O Image analysis of breast cancer immunohistochemistry-stained sections using ImageJ: an RGB-based model. Anticancer Res. 2009, 29 (12), 4995–4998. [PubMed: 20044607]

(53). Fakoor R; Ladhak F; Nazi A; Huber M In Using deep learning to enhance cancer diagnosis and classification, Proceedings of the International Conference on Machine Learning, 2013, p 28.

(54). Albain KS; Barlow WE; Shak S; Hortobagyi GN; Livingston RB; Yeh I-T; Ravdin P; Bugarini R; Baehner FL; Davidson NE; et al. Prognostic and predictive value of the 21-gene recurrence score assay in postmenopausal women with node-positive, oestrogen-receptor-positive breast cancer on chemotherapy: a retrospective analysis of a randomised trial. Lancet Oncology 2010, 11 (1), 55–65. [PubMed: 20005174]

(55). Paik S; Shak S; Tang G; Kim C; Baker J; Cronin M; Baehner FL; Walker MG; Watson D; Park T; et al. A multigene assay to predict recurrence of tamoxifen-treated, node-negative breast cancer. N. Engl. J. Med 2004, 351 (27), 2817–2826. [PubMed: 15591335]

(56). Marjanovic ND; Weinberg R A.; Chaffer, C. L. Cell plasticity and heterogeneity in cancer. Clin. Chem 2013, 59 (1), 168179.

(57). Jeon JS; Bersini S; Gilardi M; Dubini G; Charest JL; Moretti M; Kamm RD Human 3D vascularized organotypic microfluidic assays to study breast cancer cell extravasation. Proc. Natl. Acad. Sci. U. S. A 2015, 112 (1), 214–219. [PubMed: 25524628]

(58). Zheng Y; Shojaei-Baghini E; Wang C; Sun Y Microfluidic characterization of specific membrane capacitance and cytoplasm conductivity of singlecells. Biosens. Bioelectron 2013, 42, 496–502. [PubMed: 23246657]

(59). Zheng Y; Shojaei-Baghini E; Azad A; Wang C; Sun Y High-throughput biophysical measurement of human red blood cells. Lab Chip 2012, 12 (14), 2560–2567. [PubMed: 22581052]

(60). Wang K; Zhao Y; Chen D; Fan B; Lu Y; Chen L; Long R; Wang J; Chen J Specific membrane capacitance, cytoplasm conductivity and instantaneous Young's modulus of single tumour cells. Sci. Data 2017, 4, 170015. [PubMed: 28195578]

(61). Turkki R; Bychkov D; Linder N; Isola J; Joensuu H; Lundin J Exploration of tissue morphologies in breast cancer samples using unsupervised machine learning; AACR, 2017, Abstract 673.

(62). Ramarajan N; Gupta S; Perry P; Srivastava G; Kumbla A; Miller J; Feldman N; Nair N; Badwe R Abstract P1-14-01: Building an experience engine to make cancer treatment decisions using machine learning; AACR, 2017.

(63). Saib WB; Kumar P; Siwo G; Dlamini G; Singh E; Candy S; Klipin M Abstract A11: A deep learning approach for extracting clinically relevant information from pathology reports; AACR: 2017.

(64). Malta TM; Sokolov A; Gentles AJ; Burzykowski T; Poisson L; Weinstein JN; Kamińska B; Huelsken J; Omberg L; Gevaert O; et al. Machine learning identifies stemness features associated with oncogenic dedifferentiation. Cell 2018, 173 (2), 338–354 e15.. [PubMed: 29625051]

(65). Yala A; Barzilay R; Salama L; Griffin M; Sollender G; Bardia A; Lehman C; Buckley JM; Coopey SB; Polubriaginof F; et al. Using machine learning to parse breast pathology reports. Breast Cancer Res. Treat 2017, 161 (2), 203–211. [PubMed: 27826755]

(66). Bahl M; Barzilay R; Yedidia AB; Locascio NJ; Yu L; Lehman CD High-Risk Breast Lesions: A Machine Learning Model to Predict Pathologic Upgrade and Reduce Unnecessary Surgical Excision. Radiology 2018, 286, 170549.

(67). Nyberg KD; Bruce SL; Nguyen AV; Chan CK; Gill NK; Kim T-H; Sloan EK; Rowat AC Predicting cancer cell invasion by single-cell physical phenotyping. Integrative Biology 2018, 10 (4), 218–231. [PubMed: 29589844]

(68). Nyberg KD; Hu KH; Kleinman SH; Khismatullin DB; Butte MJ; Rowat AC Quantitative Deformability Cytometry: Rapid, Calibrated Measurements of Cell Mechanical Properties. Biophys. J 2017, 113 (7), 1574–1584. [PubMed: 28978449]

(69). Hoelzle DJ; Varghese BA; Chan CK; Rowat AC A microfluidic technique to probe cell deformability. J. Visualized Exp. 2014, No. 91, e51474.

(70). Babahosseini H; Ketene AN; Schmelz EM; Roberts PC; Agah M Biomechanical profile of cancer stem-like/tumor-initiating cells derived from a progressive ovarian cancer model. Nanomedicine 2014, 10 (5), e1013–e1019.

(71). Lyon C; Mill C; Tsaousi A; Williams H; George S Regulation of VSMC behavior by the cadherin-catenin complex. Front. Biosci., Landmark Ed 2011, 16, 644–673. [PubMed: 21196194]

(72). Sarrió D; Rodriguez-Pinilla SM; Hardisson D; Cano A; Moreno-Bueno G; Palacios J Epithelial-mesenchymal transition in breast cancer relates to the basal-like phenotype. Cancer Res. 2008, 68 (4), 989–997. [PubMed: 18281472]

(73). Nieman MT; Prudoff RS; Johnson KR; Wheelock MJ N-cadherin promotes motility in human breast cancer cells regardless of their E-cadherin expression. J. Cell Biol 1999, 147 (3), 631–644. [PubMed: 10545506]

(74). Subik K; Lee J-F; Baxter L; Strzepek T; Costello D; Crowley P; Xing L; Hung M-C; Bonfiglio T; Hicks DG; et al. The expression patterns of ER, PR, HER2, CK5/6, EGFR, Ki-67 and AR by immunohistochemical analysis in breast cancer cell lines. Breast Cancer: Basic Clin. Res 2010, 4, 35.

(75). Chavez KJ; Garimella SV; Lipkowitz S Triple negative breast cancer cell lines: one tool in the search for better treatment of triple negative breast cancer. Breast Dis. 2011, 32 (1–2), 35.

(76). Meacham CE; Morrison SJ Tumor heterogeneity and cancer cell plasticity. Nature 2013, 501 (7467), 328. [PubMed: 24048065]

(77). DeSantis CE; Ma J; Goding Sauer A; Newman LA; Jemal A Breast cancer statistics, 2017, racial disparity in mortality by state. Ca-Cancer J. Clin 2017, 67 (6), 439–448. [PubMed: 28972651]

(78). Ellis L; Canchola AJ; Spiegel D; Ladabaum U; Haile R; Gomez SL Racial and Ethnic Disparities in Cancer Survival: The Contribution of Tumor, Sociodemographic, Institutional, and Neighborhood Characteristics. J. Clin. Oncol 2018, 36, 25. [PubMed: 29035642]

(79). Jemal A; Robbins AS; Lin CC; Flanders WD; DeSantis CE; Ward EM; Freedman RA Factors That Contributed to Black-White Disparities in Survival Among Nonelderly Women With Breast Cancer Between 2004 and 2013. J. Clin. Oncol 2018, 36, 14. [PubMed: 29035645]

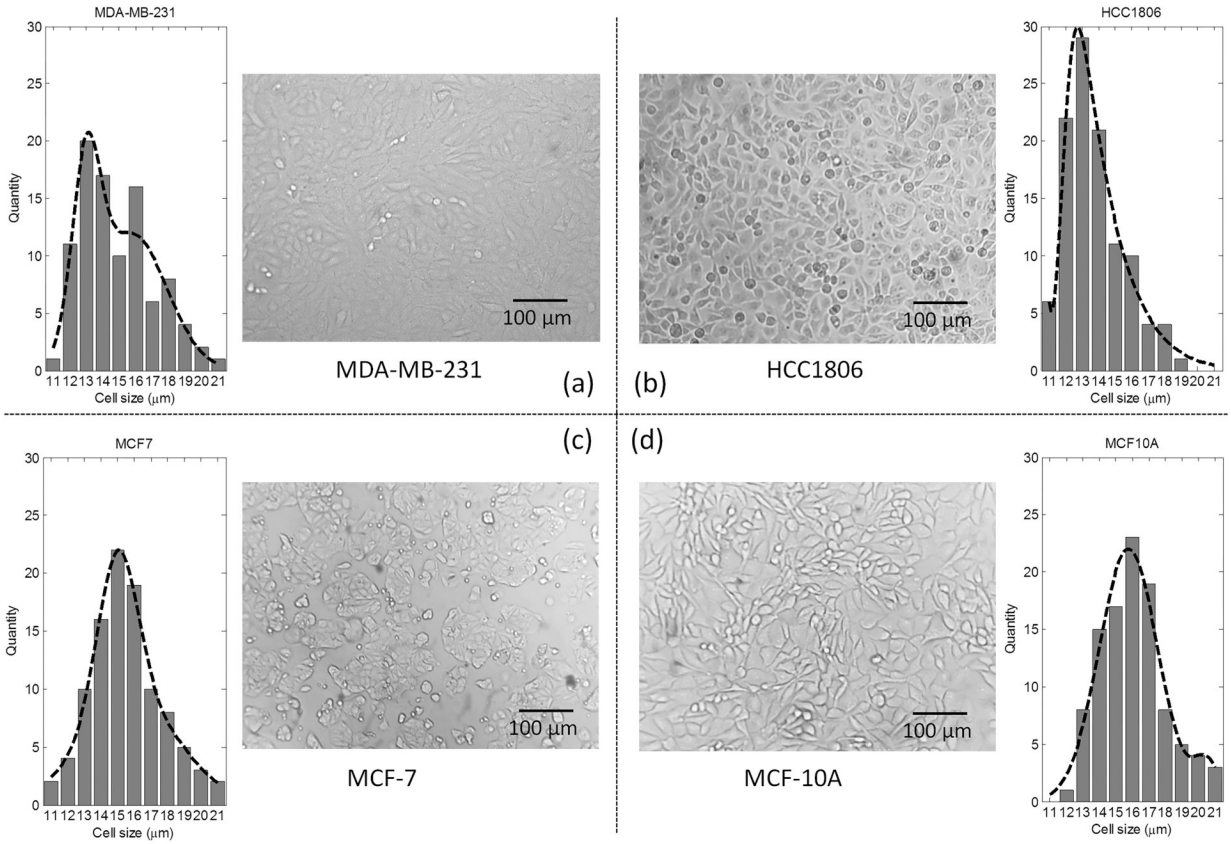

Figure 1.

Cell morphology before trypsinization and cell size distribution: (a) MDA-MB-231; (b) HCC-1806; (c) MCF-7; (d) MCF-10A.

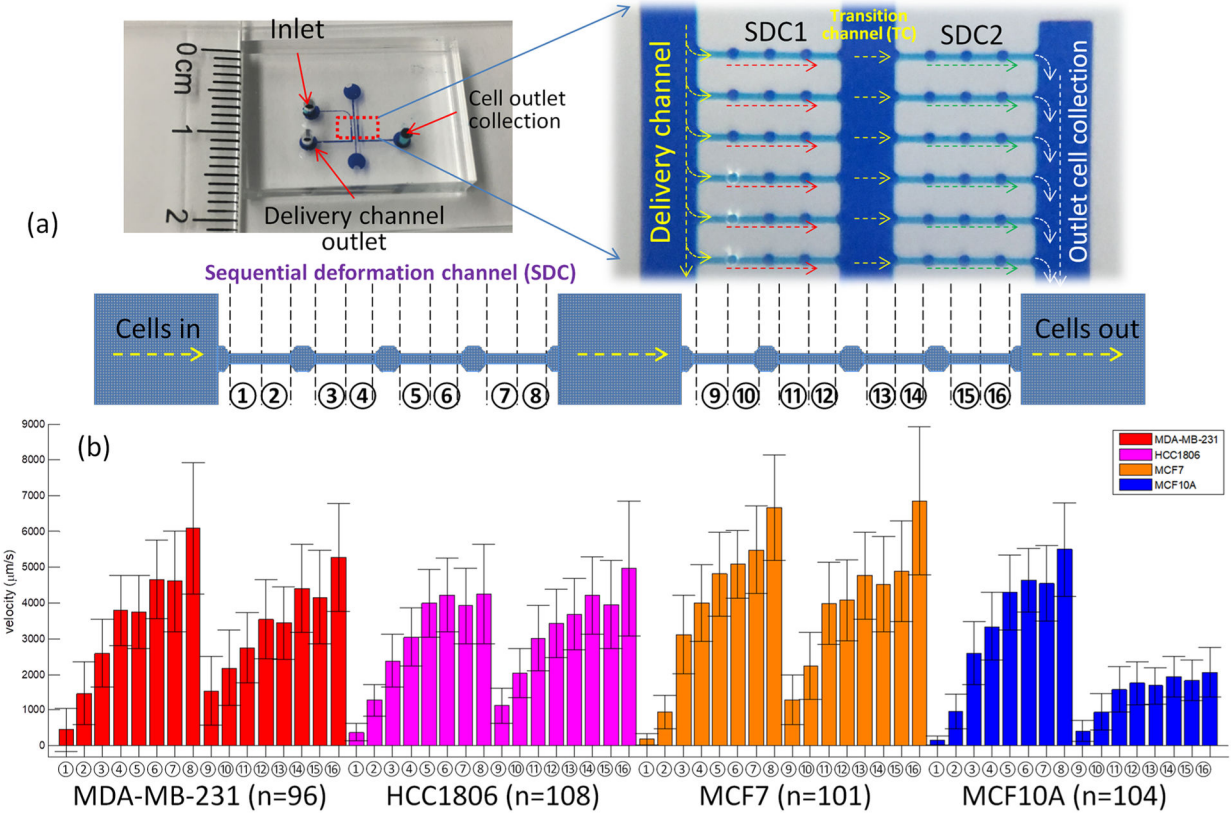

Figure 2.

(a) High-throughput multiconstriction microfluidic channel device and channel labeling. (b) Velocity at different segments of four cell lines; error bars represent standard deviation.

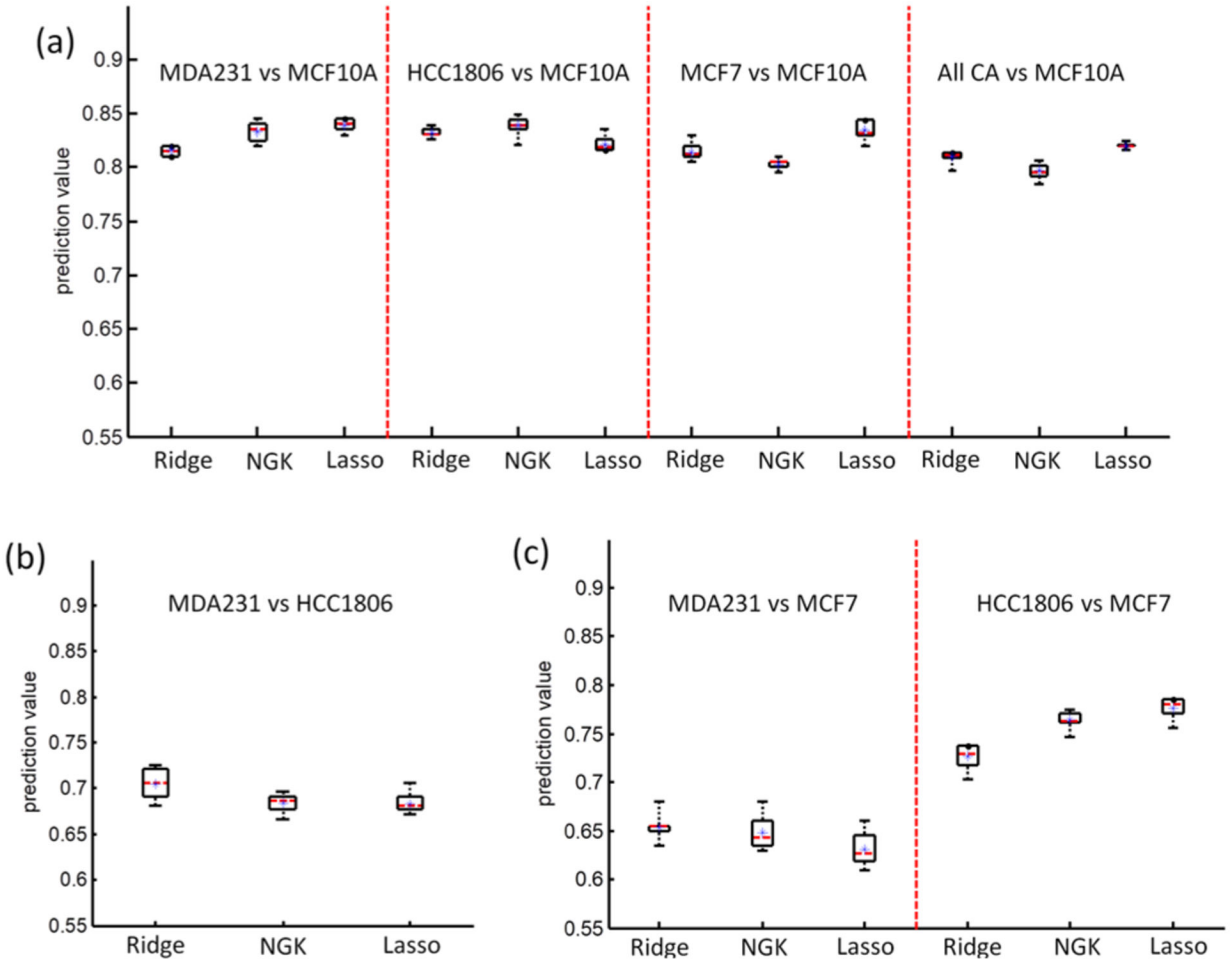

Figure 3.

Prediction values of (a) comparing cancer cell lines MDA-MB-231, HCC-1806, and MCF-7 to normal cell line MCF-10A; (b) comparing MDA-MB-231 and HCC-1806; (c) comparing TNBC cell lines MDA-MB-231 and HCC-1806 to ER+/PR+/Her2− cell line MCF-7.

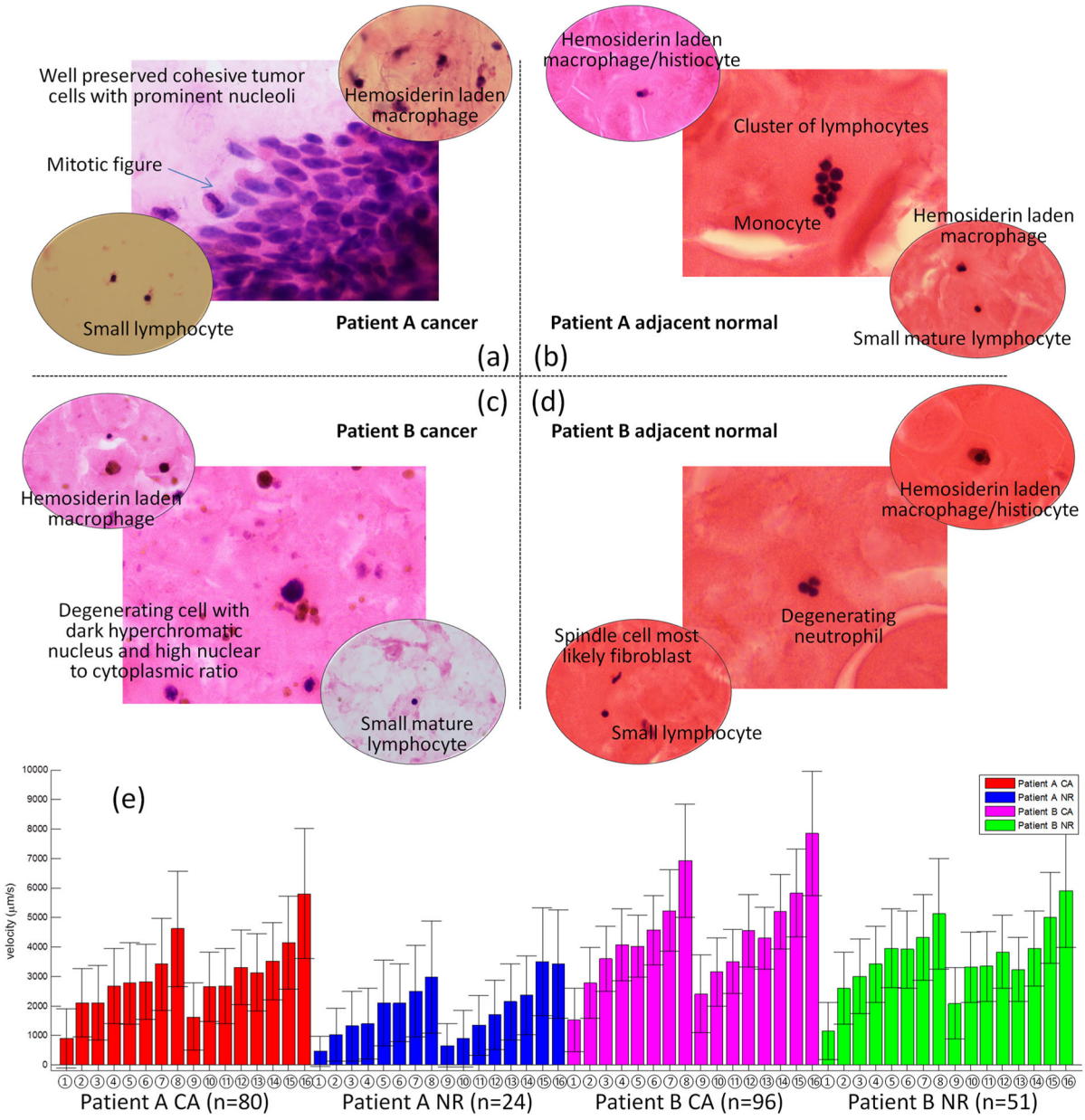

Figure 4.

H&E stained slides of cell suspensions: (a) patient A cancer (CA) tissue; (b) patient A adjacent normal (NR) tissue; (c) patient B CA tissue; (d) patient B NR tissue. (e) Velocity profiles for patient A (CA, red; NR, blue) and patient B (CA, violet; NR, lime).

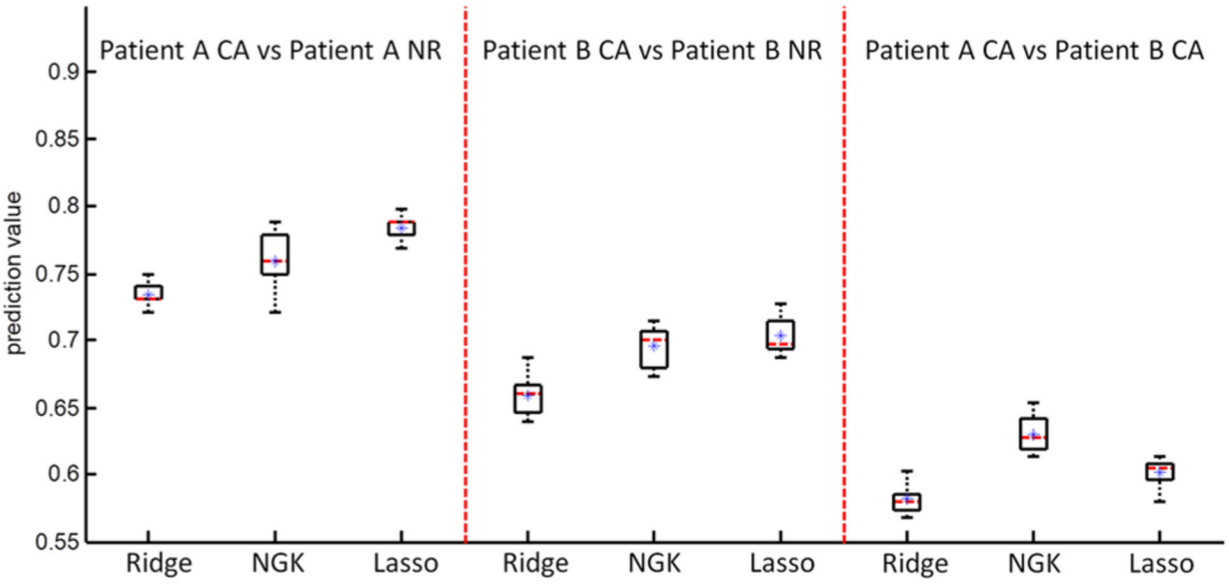

Figure 5.

Prediction values of comparing the CA and adjacent NR cells in patient A, CA and adjacent NR cells in patient B, and comparing the CA cells in patients A and B.

Table 1.

Average Size and Cell Type Distribution in Patient Cancer Samples

	patient A		patient B	
cell types	**cell size (μm)[a]**	**cell counts (%, *n*[b])**	**cell size (μm)[a]**	**cell counts (%, *n*[b])**
epithelial	18.6 ± 7.1	37.6%, 34	16.0 ± 3.6	29.4%, 17
lymphoid	10.5 ± 1.7	39.8%, 14	8.4 ± 3.5	32.4%, 34
M/H	14.3 ± 3.7	N/A,[c] 3	11.1 ± 1.7	25.0%, 12

[a] Error is one standard deviation.

[b] *n* is cell counts.

[c] Sample size from patient A is limited (only 3 cells observed in IHC study).